Continuous hydrothermal synthesis in supercritical conditions as a novel process for the elaboration of Y-doped BaZrO3

Mélanie François, Frédéric Demoisson, Mohamed Sennour, Gilles Caboche

Continuous hydrothermal synthesis in supercritical conditions as a novel process for the elaboration of Y-doped $BaZrO_3$

Mélanie François*[1], Frédéric Demoisson[1], Mohamed Sennour[2] and Gilles Caboche[1]

[1] Laboratoire Interdisciplinaire Carnot de Bourgogne, FCLAB, ICB-UMR6303, CNRS – Université de Bourgogne Franche-Comté, 9 Avenue Savary, BP47870 21078 DIJON Cedex, France

[2] Centre des matériaux – MINES ParisTech, 63-65 rue Henri Auguste Desbruères, BP 87 91003 Evry Cedex, France

* Correspondence : melanie.francois@u-bourgogne.fr

Abstract: The present work describes a novel process for the elaboration of a ceramic material. Y-doped barium zirconate, an electrolyte material for Protonic Ceramic Fuel cell, was synthesized by a continuous hydrothermal process in supercritical conditions (410°C/30.0MPa) using nitrate precursors and NaOH reactants. The use of supercritical water allowed the formation of particles of about 50 nm in diameter with a narrow size distribution. X-Ray Diffraction examination revealed that a major perovskite phase with few $BaCO_3$ and YO(OH) impurities was obtained. $BaCO_3$ is assumed to form due to faster kinetics than Y-doped $BaZrO_3$ resulting in a Ba-deficient perovskite phase. The Ba-deficiency limits the incorporation of yttrium into the perovskite structure. However, a thermal treatment at 1000 °C for 1 hour allows to homogenize the composition and thus to obtain the compound $Ba_{1.01}Zr_{0.85}Y_{0.15}O_{3-\delta}$.

Keywords: Hydrothermal synthesis; Protonic Ceramic Fuel Cell; Nanoparticles; Supercritical water; Y-doped $BaZrO_3$.

1. Introduction

Finding new clean and efficient ways to generate energy has become a major global challenge. For a few years now, Protonic Ceramic Fuel Cells (PCFCs) have attracted much attention in the field of hydrogen energy. Contrary to Solid Oxide Fuel Cells that operate at a temperature above 600 °C and where the oxygen ions are the charge carriers, PCFCs use protons. Indeed, the lower activation energy of proton diffusion compared to that of the oxygen ion allows to decrease the operating

temperature down to the 400 – 600 °C range[1]. Among the different electrolyte materials for PCFCs, $BaCeO_3$ and $BaZrO_3$ have attracted much attention [2–4].

$BaCeO_3$-based oxides are currently the most commonly chosen electrolyte material for PCFC [5,6]. It is generally reported that doped-$BaCeO_3$ exhibits the highest protonic conductivity among the perovskite-type materials [7–9]. However, $BaCeO_3$-based perovskites exhibit low stability in H_2O and/or CO_2 containing atmosphere which limits their practical application [10,11]. On the contrary, doped $BaZrO_3$ exhibits excellent chemical stability [12]. The substitution of zirconium by yttrium allows to achieve acceptable electrical conductivity up to 10^{-3} $S.cm^{-1}$ [13,14]. However, the highly refractive nature of $BaZr_{1-x}Y_xO_{3-\delta}$ (noted BZY) leads to the requirement of a high synthesis temperature (1400 °C) for the classical solid state reaction method and to an even higher (1600 – 1700 °C) sintering temperature [15,16].

In this work, a continuous hydrothermal process developed at the ICB laboratory is proposed to elaborate the electrolyte material [17]. The supercritical hydrothermal synthesis of metal oxide particles using a continuous flow reactor was first proposed by Adschiri *et al*. in 1992 [18]. This process presents several advantages such as a precise control of the morphology and the size of the particles with a narrow size distribution [19–21]. Furthermore, in supercritical water, inorganic compounds become insoluble leading to the formation of hydroxide nuclei which are immediately dehydrated to form ultrafine particles [22]. Another important advantage of using supercritical water with a continuous flow is the short reaction time leading to the possible formation of metastable and highly doped structures [23,24].

The synthesis of $BaZrO_3$ by the continuous hydrothermal process was investigated by several groups in the past decade. For example, Aimable *et al*. studied the influence of the nature of the precursors, the pH and the temperature on the synthesis of $BaZrO_3$ [25]. Yoko *et al*. studied the formation mechanism of $BaZrO_3$ in supercritical water. They suspected the formation of Ba-deficient particles with a shell of ZrO(OH) at the early stage of the precipitation followed by an uptake of Ba^{2+} up to Ba/Zr=1 [26]. In 2016, the same group used *in situ* X-ray diffraction to study and support the previous mechanism [27].

However, few studies focus on doped $BaZrO_3$ material elaborated by this method, and, to the authors' knowledge, no studies on Y-doped $BaZrO_3$ have been conducted. Then, this work aims to

investigate the feasibility of the elaboration of $BaZr_{1-x}Y_xO_{3-\delta}$ by supercritical hydrothermal process using a continuous flow reactor.

2. Materials and Methods

2.1. Continuous process

The continuous process can be used up to 600 °C/35.0 MPa. Indeed, for water, the critical temperature/critical pressure values are 374 °C/22.1 MPa, this set-up can work in supercritical conditions. For the experiments, the syntheses were carried out at 410 °C/30.0 MPa. A solution of metallic precursors ($Ba(NO_3)_2$, $ZrO(NO_3)_2{\cdot}6H_2O$ and $Y(NO_3)_3{\cdot}6H_2O$ purchased from Sigma-Aldrich) is prepared by following the stoichiometry of the target composition by dissolution in deionized water and homogenized with an ultrasonic rod, the concentration is 5×10^{-2} mol L^{-1} for Ba^{2+}, 4×10^{-2} mol L^{-1} for Zr^{4+} and 1×10^{-2} mol L^{-1} for Y^{3+}. A second solution composed of sodium hydroxide at 3×10^{-1} mol L^{-1} was employed in order to avoid the formation of ZrO_2 [25]. **Figure 1** shows the scheme of the continuous set-up. Container (a), at the beginning of the process, holds the aqueous solution of metal cations, container (b) holds the solution of sodium hydroxide and the third container (c) holds the distilled water. The reactor consists of a “pipe to pipe” cylinder with a total volume of 25 mL, the inner diameter of the external pipe is 10 mm. Pressurized solutions (a) and (b) are brought to the reactor inlet at room temperature by high-pressure pumps. Pressurized demineralized water is pre-heated and brought counter-currently through the internal pipe of the reactor so that the three solutions meet at the mixing zone. The resulting solution is evacuated through the external pipe where the reactions leading to the formation of metal oxides take place. The flow rate of the three solutions is set to around 10 mL min^{-1} per solution, the final flow measured at the end of the set-up (after the back pressure regulator) varies between 30 and 35 $mL.min^{-1}$. The residence time into the reactor under supercritical conditions is of the order of few seconds (determined by Computational Fluid Dynamics calculations) [28]. At the reactor outlet, a cooling system stops the germination and growth stages. A filtration system at the end of the device captures the agglomerated particles that are added to the suspension obtained after the back-pressure regulator. The particles sediment at the bottom of the beaker, the surfactant is siphoned off and distilled water is added to wash the particles. This operation is repeated until a

neutral pH is obtained. The supernatant water is siphoned off one last time and the suspension is dried in an oven at 80 °C for three days to obtain a powder.

2.2. Characterization methods

X-Ray Diffraction (XRD) analysis was conduct on a Bruker D2 Phaser coupled with linear detector Lynxeye_XE_T using Cu Kα radiation. The obtained XRD pattern was refined by the Rietveld method using the Fullprof software. The microstructure was investigated by transmission electron microscopy (TEM) on a ThermoFisher FEI Tecnai F20. The chemical composition was analyzed by scanning electron microscopy (SEM) on a Hitachi SU1510 coupled with a Bruker XFlash6I10 energy-dispersive X-ray (EDX) analyzer. The collected peaks for EDX quantification were the L-series of Ba, Zr and Y and the K-series of O. EDX investigations were conducted on 16 different agglomerates with an area of measurement from 2.5 µm × 2.5µm to 5µm × 5 µm. The Brunauer, Emmett and Teller (BET) measurement was carried out on a Micromeritics TriStar 3020. Particle size distribution (PSD) was evaluated using the Dynamic Light Scattering method using Mie theory calculation with a Malvern Microsizer 2000 laser granulometer coupled with a hydro 2000MU dispersion unit using ultrasound.

3. Results and discussion

Among the Y-doped $BaZrO_3$ materials, $BaZr_{0.8}Y_{0.2}O_{3-\delta}$ appears to be the best composition. The protonic conductivity increases with the Y content up to a substitution of 20 % before decreasing due to structural distortion and proton trapping [29,30]. Thus, $BaZr_{0.8}Y_{0.2}O_{3-\delta}$ was the target composition. The chemical reaction yield varies from 60.5 % to 70 % with an average value of 66.5 %, the productivity depends on the final flow measured after the back pressure regulator and varies from 5.5 to 6.8 $g.h^{-1}$, about 23.5 g was produced per synthesis.

Figure 2 shows the volume and number PSD of the synthesized powder. The volume PSD (Figure 1.a) exhibit a quadrimodal distribution with mean sizes at around 0.1 µm, 1.7 µm, 14 µm and 210 µm. The obtained D_{10}, D_{50} and D_{90} are 0.817 µm, 4.570 µm and 35.73 µm respectively suggesting that the elementary grains are highly agglomerate. **Figure 3** shows the TEM micrograph of the synthesized powder. As suggested by the PSD analysis, the particles with a nearly spherical morphology are agglomerated. The particle size varies from 10 nm to 315 nm on this micrograph with a median value of 48 nm (evaluation on 50 particles).

The X-ray diffractogram of the obtained powder is shown in **Figure 4**. The major phase obtained has a perovskite cubic structure with Pm-3m space group. $BaCO_3$, with an orthorhombic Pnma structure, and YO(OH), with a monoclinic $P2_1/m$ structure as secondary phases were detected. Rietveld refinement was performed on the diffractogram, the determined phase percentages are 86.2, 10.6 and 3.1 wt% for BZY, $BaCO_3$ and YO(OH) respectively. The average crystallite size of the perovskite phase was evaluated from the integral width of the diffraction peaks and is 53 nm. This value is in agreement with the 48 nm obtained from TEM analysis and with the 47.3 ± 0.2 nm calculated from the 20.74 ± 0.06 $m^2 g^{-1}$ specific surface area obtained by BET measurement. The refined lattice parameter for the perovskite cubic phase is 4.2015 Å, this value is lower than those reported in the literature for $BaZr_{0.8}Y_{0.2}O_{3-\delta}$ suggesting that a part of Y is not in the perovskite phase leading to the formation of YO(OH). As a comparison, Sun *et al.* obtained a lattice parameter of 4.2048 Å for $BaZr_{0.8}Y_{0.2}O_{3-\delta}$ prepared by combustion method, Nuñez et al. obtained a lattice parameter of 4.2067 Å for $BaZr_{0.8}Y_{0.2}O_{3-\delta}$ prepared by a modified Pechini method and Sazinas *et al*. obtained a lattice parameter of 4.2151 Å for $BaZr_{0.8}Y_{0.2}O_{3-\delta}$ prepared by spray pyrolysis and sintered at 1600 °C [31–33]. In order to investigate the origin of lattice parameter deviation, a comparison with undoped $BaZrO_3$ elaborated by the same method was carried out. The refined lattice parameter is 4.1939 Å, this value agrees well with the 4.1930 Å and the 4.1943 Å obtained by the Nuñez group and the Akbarzadeh group [32,34]. Then, this synthesis method does not appear to particularly generate defects or nano-size effects that affect the lattice parameter. Moreover, the increase in the lattice parameter for Y-doped $BaZrO_3$ compared to the non-doped sample well evidence the Y doping. However, the amount of Y cannot be quantified by XRD since the synthesis route implement several defects or structural distortions that affect the lattice parameter value, for example, values of lattice parameter for $BaZr_{0.9}Y_{0.1}O_{3-\delta}$ differ from 4.193 Å to 4.2101 Å [33,35–38].

In order to determine the composition of the BZY powder as-synthesized, EDX investigations were conducted on several agglomerates. Ba, Zr, Y and O elements were detected, for the following interpretation, Ba is assumed to belong to the A-site of the perovskite while Zr and Y are supposed to occupy the B-site of the perovskite. **Figure 5** shows a) the obtained A-site/B-site ratios and b) the obtained Y/(Zr+Y) ratios and the corresponding number of agglomerates per interval. The as-synthesized powder exhibits a wide range of A-site/B-site ratio, from 0.70 to 1.33, with a strong tendency for the Ba-deficient composition. In order to homogenize the composition, a heat

treatment at 1000 °C for 1 hour was applied to the powder. The resulting distribution of A-site/B-site ratio is narrower, the lower value is 0.92 and the biggest value is 1.08 with an average value equal to 1.01. Then, the thermal treatment at 1000°C effectively homogenizes the composition. Moreover, a study of Haile group showed that $BaCO_3$ decomposition leads to the compensation of the Ba sub-stoichiometry during sintering [39]. Since $BaCO_3$ decomposition (reaction 1) occurs at around 1000 °C [40], it can reasonably be assumed that the increase of the A-site/B-site ratio in the annealed powder is due to the Ba uptake from $BaCO_3$. The integration of Ba in the BZY structure is described in Kröger – Vink notation in reaction 2.

$$BaCO_3 \rightarrow BaO + CO_2 \qquad \text{Reaction 1}$$

$$BaO + V_{Ba}'' + V_O^{\bullet\bullet} \rightarrow Ba_{Ba}^{\times} + O_O^{\times} \qquad \text{Reaction 2}$$

The Y/(Zr+Y) ratio values of the as-synthesized powder cover an interval of 0.08 to 0.25 with an average value of 0.14, this ratio is lower than the expected 0.20. Yamazaki *et al.* and Magrez *et al*. have shown that yttria exsolution in Ba-deficient BZY compounds during sintering is due to the Ba sub-stoichiometry [41,42]. It can then be assumed that, in hydrothermal synthesis, the Ba-deficiency caused by the kinetics of the $BaCO_3$ formation faster than the BZY formation hinders the incorporation of more than 14 % of Y in the BZY structure. After thermal treatment, the distribution of Y/(Zr+Y) is substantially the same as before, covering an interval from 0.07 to 0.24 with an average value of 0.15. Because of the high occupancy rate of the B-site of the perovskite, yttrium from YO(OH) cannot integrate the perovskite structure and react at 450 °C to form Y_2O_3 according to reaction 3 [43]:

$$2\ YO(OH) \rightarrow Y_2O_3 + H_2O \qquad \text{Reaction 3}$$

4. Conclusions

The hydrothermal synthesis of $BaZr_{1-x}Y_xO_{3-\delta}$ was carried out in supercritical water (410 °C/30.0 MPa) using a continuous flow reactor. This process allows the elaboration of nanoparticles of about 50 nm in diameter with great productivity (5.5 – 6.8 g h^{-1}), an average chemical reaction yield of 66.5 % and high reproducibility. XRD characterization revealed the presence of $BaCO_3$ and few YO(OH) impurities. It is assumed that $BaCO_3$ formation occurs due to faster kinetics compared to that of BZY formation. EDX study showed the obtaining of highly Ba-deficient perovskite and a substitution rate of Zr by Y of about 14%. However, a thermal treatment at 1000 °C for 1 hour

allowed the homogenization of the composition resulting in a $Ba_{1.01}Zr_{0.85}Y_{0.15}O_{3-\delta}$ perovskite phase. In summary, this continuous hydrothermal synthesis in supercritical conditions is highly promising and extensive research on controlling the synthesis parameters would greatly broaden the possibilities for elaborating advanced ceramic materials at low temperature.

Funding: This research was funded in part by the Regional Council of Bourgogne Franche-Comté, the FEDER and the Graduate School EIPHI (Contract ANR-17-EURE-0002).

Acknowledgments: The authors thank the ESIREM Engineering college for the SEM experimentations.

Conflicts of Interest: The authors declare no conflict of interest.

References

[1] Y. Meng, J. Gao, Z. Zhao, J. Amoroso, J. Tong, K.S. Brinkman, Review: recent progress in low-temperature proton-conducting ceramics, J Mater Sci. 54 (2019) 9291–9312. https://doi.org/10.1007/s10853-019-03559-9.

[2] S. Hossain, A.M. Abdalla, S.N.B. Jamain, J.H. Zaini, A.K. Azad, A review on proton conducting electrolytes for clean energy and intermediate temperature-solid oxide fuel cells, Renewable and Sustainable Energy Reviews. 79 (2017) 750–764. https://doi.org/10.1016/j.rser.2017.05.147.

[3] A. Nowick, High-temperature protonic conductors with perovskite-related structures, Solid State Ionics. 77 (1995) 137–146. https://doi.org/10.1016/0167-2738(94)00230-P.

[4] H. Dai, H. Kou, H. Wang, L. Bi, Electrochemical performance of protonic ceramic fuel cells with stable BaZrO3-based electrolyte: A mini-review, Electrochemistry Communications. 96 (2018) 11–15. https://doi.org/10.1016/j.elecom.2018.09.001.

[5] X. Xu, L. Bi, Proton-conducting electrolyte materials, in: Intermediate Temperature Solid Oxide Fuel Cells, Elsevier, 2020: pp. 81–111. https://doi.org/10.1016/B978-0-12-817445-6.00003-X.

[6] L. Bi, Z. Tao, C. Liu, W. Sun, H. Wang, W. Liu, Fabrication and characterization of easily sintered and stable anode-supported proton-conducting membranes, Journal of Membrane Science. 336 (2009) 1–6. https://doi.org/10.1016/j.memsci.2009.03.042.

[7] K.D. Kreuer, Proton-Conducting Oxides, Annual Review of Materials Research. 33 (2003) 333–359. https://doi.org/10.1146/annurev.matsci.33.022802.091825.

[8] K.H. Ryu, S.M. Haile, Chemical stability and proton conductivity of doped BaCeO3–BaZrO3 solid solutions, Solid State Ionics. 125 (1999) 355–367. https://doi.org/10.1016/S0167-2738(99)00196-4.

[9] S. Wang, J. Shen, Z. Zhu, Z. Wang, Y. Cao, X. Guan, Y. Wang, Z. Wei, M. Chen, Further optimization of barium cerate properties via co-doping strategy for potential application as proton-conducting solid oxide fuel cell electrolyte, Journal of Power Sources. 387 (2018) 24–32. https://doi.org/10.1016/j.jpowsour.2018.03.054.

[10] H. Matsumoto, Y. Kawasaki, N. Ito, M. Enoki, T. Ishihara, Relation Between Electrical Conductivity and Chemical Stability of BaCeO[sub 3]-Based Proton Conductors with Different Trivalent Dopants, Electrochemical and Solid-State Letters. 10 (2007) B77. https://doi.org/10.1149/1.2458743.

[11] W. Münch, Proton diffusion in perovskites: comparison between BaCeO3, BaZrO3, SrTiO3, and CaTiO3 using quantum molecular dynamics, Solid State Ionics. 136–137 (2000) 183–189. https://doi.org/10.1016/S0167-2738(00)00304-0.

[12] J.-H. Kim, Y.-M. Kang, M.-S. Byun, K.-T. Hwang, Study on the chemical stability of Y-doped BaCeO3−δ and BaZrO3−δ films deposited by aerosol deposition, Thin Solid Films. 520 (2011) 1015–1021. https://doi.org/doi:10.1016/j.tsf.2011.08.013.

[13] E. Fabbri, L. Bi, D. Pergolesi, E. Traversa, Towards the Next Generation of Solid Oxide Fuel Cells Operating Below 600 °C with Chemically Stable Proton-Conducting Electrolytes, Advanced Materials. 24 (2012) 195–208. https://doi.org/10.1002/adma.201103102.

[14] D. Yun, J. Kim, S.-J. Kim, J.-H. Lee, J.-N. Kim, H. Yoon, J. Yu, M. Kwak, H. Yoon, Y. Cho, C.-Y. Yoo, Structural and Electrochemical Properties of Dense Yttria-Doped Barium Zirconate Prepared by Solid-State Reactive Sintering, Energies. 11 (2018) 3083–3099. https://doi.org/10.3390/en11113083.

[15] L. Bi, E. Traversa, Synthesis strategies for improving the performance of doped-$BaZrO_3$ materials in solid oxide fuel cell applications, J. Mater. Res. 29 (2014) 1–15. https://doi.org/10.1557/jmr.2013.205.

[16] F.J.A. Loureiro, N. Nasani, G.S. Reddy, N.R. Munirathnam, D.P. Fagg, A review on sintering technology of proton conducting BaCeO3-BaZrO3 perovskite oxide materials for Protonic Ceramic Fuel Cells, Journal of Power Sources. 438 (2019) 226991. https://doi.org/10.1016/j.jpowsour.2019.226991.

[17] D. Aymes, M. Ariane, F. Bernard, H. Muhr, F. Demoisson, Counter-current flow reactor with heat transfer for hydrothermolytic synthesis, WO 2011010056A1, 2011.

[18] T. Adschiri, K. Kanazawa, K. Arai, Rapid and Continuous Hydrothermal Crystallization of Metal Oxide Particles in Supercritical Water, J American Ceramic Society. 75 (1992) 1019–1022. https://doi.org/10.1111/j.1151-2916.1992.tb04179.x.

[19] F. Demoisson, R. Piolet, F. Bernard, Hydrothermal Synthesis of ZnO Crystals from $Zn(OH)_2$ Metastable Phases at Room to Supercritical Conditions, Crystal Growth & Design. 14 (2014) 5388–5396. https://doi.org/10.1021/cg500407r.

[20] C. Pighini, D. Aymes, N. Millot, L. Saviot*, Low-frequency Raman characterization of size-controlled anatase TiO2 nanopowders prepared by continuous hydrothermal syntheses, Journal of Nanoparticle Research. 9 (2007) 309–315. https://doi.org/10.1007/s11051-005-9061-6.

[21] G. Philippot, E.D. Boejesen, C. Elissalde, M. Maglione, C. Aymonier, B.B. Iversen, Insights into $BaTi_{1-y}Zr_yO_3$ ($0 \leq y \leq 1$) Synthesis under Supercritical Fluid Conditions, Chemistry of Materials. 28 (2016) 3394–3400. https://doi.org/DOI: 10.1021/acs.chemmater.6b00635.

[22] F. Demoisson, Influence of the pH on the ZnO nanoparticle growth in supercritical water: Experimental and simulation approaches, Journal of Supercritical Fluids. 95 (2014) 75–83. https://doi.org/10.1016/j.supflu.2014.08.007.

[23] Y. Zhu, G. Seong, T. Noguchi, A. Yoko, T. Tomai, S. Takami, T. Adschiri, Highly Cr-Substituted CeO_2 Nanoparticles Synthesized Using a Non-equilibrium Supercritical Hydrothermal Process: High Oxygen Storage Capacity Materials Designed for a Low-Temperature Bitumen Upgrading Process, ACS Appl. Energy Mater. 3 (2020) 4305–4319. https://doi.org/10.1021/acsaem.0c00026.

[24] A. Yoko, G. Seong, T. Tomai, T. Adschiri, Continuous Flow Synthesis of Nanoparticles Using Supercritical Water: Process Design, Surface Control, and Nanohybrid Materials, KONA. 37 (2020) 28–41. https://doi.org/10.14356/kona.2020002.

[25] A. Aimable, B. Xin, N. Millot, D. Aymes, Continuous hydrothermal synthesis of nanometric BaZrO3 in supercritical water, Journal of Solid State Chemistry. 181 (2008) 183–189. https://doi.org/10.1016/j.jssc.2007.11.015.

[26] A. Yoko, M. Akizuki, Y. Oshima, Formation mechanism of barium zirconate nanoparticles under supercritical hydrothermal synthesis, Journal of Nanoparticle Research. 16 (2014). https://doi.org/10.1007/s11051-014-2330-5.

[27] A. Yoko, M. Akizuki, N. Hirao, S. Kohara, M. Kumar, N. Umezawa, T. Ohno, Y. Oshima, In situ X-ray diffraction for millisecond-order dynamics of BaZrO 3 nanoparticle formation in supercritical water, The Journal of Supercritical Fluids. 107 (2016) 746–752. https://doi.org/10.1016/j.supflu.2015.08.002.

[28] F. Demoisson, M. Ariane, A. Leybros, H. Muhr, F. Bernard, Design of a reactor operating in supercritical water conditions using CFD simulations. Examples of synthesized nanomaterials, The Journal of Supercritical Fluids. 58 (2011) 371–377. https://doi.org/10.1016/j.supflu.2011.07.001.

[29] D. Han, N. Hatada, T. Uda, Chemical Expansion of Yttrium-Doped Barium Zirconate and Correlation with Proton Concentration and Conductivity, J. Am. Ceram. Soc. 99 (2016) 3745–3753. https://doi.org/10.1111/jace.14377.

[30] E. Fabbri, D. Pergolesi, S. Licoccia, E. Traversa, Does the increase in Y-dopant concentration improve the proton conductivity of BaZr1−xYxO3−δfuel cell electrolytes?, Solid State Ionics. 181 (2010) 1043–1051. https://doi.org/doi:10.1016/j.ssi.2010.06.007.

[31] W. Sun, M. Liu, W. Liu, Chemically Stable Yttrium and Tin Co-Doped Barium Zirconate Electrolyte for Next Generation High Performance Proton-Conducting Solid Oxide Fuel Cells, Adv. Energy Mater. 3 (2013) 1041–1050. https://doi.org/10.1002/aenm.201201062.

[32] G. Nuñez, M.J. Balanay, R.B.M. Cervera, Preparation of Y-Doped $BaZrO_3$ Proton Conducting Solid Electrolyte via Modified Low Temperature Pechini Method, AMR. 1098 (2015) 86–91. https://doi.org/10.4028/www.scientific.net/AMR.1098.86.

[33] R. Sažinas, C. Bernuy-López, M.-A. Einarsrud, T. Grande, Effect of CO_2 Exposure on the Chemical Stability and Mechanical Properties of $BaZrO_3$ -Ceramics, J. Am. Ceram. Soc. 99 (2016) 3685–3695. https://doi.org/10.1111/jace.14395.

[34] A.R. Akbarzadeh, I. Kornev, C. Malibert, L. Bellaiche, J.M. Kiat, Combined theoretical and experimental study of the low-temperature properties of BaZrO 3, Phys. Rev. B. 72 (2005) 205104. https://doi.org/10.1103/PhysRevB.72.205104.

[35] M.F. Hoedl, E. Makagon, I. Lubomirsky, R. Merkle, E.A. Kotomin, J. Maier, Impact of point defects on the elastic properties of BaZrO3: Comprehensive insight from experiments and ab

294 initio calculations, Acta Materialia. 160 (2018) 247–256.
295 https://doi.org/10.1016/j.actamat.2018.08.042.
296 [36] S.B.C. Duval, P. Holtappels, U.F. Vogt, U. Stimming, T. Graule, Characterisation of $BaZr_{0.9}Y_{0.1}O_{3-\delta}$ Prepared by Three Different Synthesis Methods: Study of the Sinterability and the
298 Conductivity, Fuel Cells. 9 (2009) 613–621. https://doi.org/10.1002/fuce.200800170.
299 [37] T. Schober, Water vapor solubility and electrochemical characterization of the high
300 temperature proton conductor BaZr0.9Y0.1O2.95, Solid State Ionics. 127 (2000) 351–360.
301 https://doi.org/10.1016/S0167-2738(99)00283-0.
302 [38] Tsvetkov, Ivanov, Malyshkin, Sereda, Zuev, Thermoelectric Behavior of BaZr0.9Y0.1O3−d
303 Proton Conducting Electrolyte, Membranes. 9 (2019) 120.
304 https://doi.org/10.3390/membranes9090120.
305 [39] Y. Yamazaki, R. Hernandez-Sanchez, S.M. Haile, High Total Proton Conductivity in
306 Large-Grained Yttrium-Doped Barium Zirconate, Chem. Mater. 21 (2009) 2755–2762.
307 https://doi.org/10.1021/cm900208w.
308 [40] I. Arvanitidis, D. Sichen, S. Seetharaman, A Study of the Thermal Decomposition of BaC03,
309 Metallurgical and Materials Transactions B. 27B (1996) 409–416.
310 [41] Y. Yamazaki, R. Hernandez-Sanchez, S.M. Haile, Cation non-stoichiometry in yttrium-doped
311 barium zirconate: phase behavior, microstructure, and proton conductivity, Journal of
312 Materials Chemistry. 20 (2010) 8158–8166. https://doi.org/DOI: 10.1039/c0jm02013c.
313 [42] A. Magrez, T. Schober, Preparation, sintering, and water incorporation of proton conducting
314 Ba0.99Zr0.8Y0.2O3Àd: comparison between three different synthesis techniques, Solid State
315 Ionics. 175 (2004) 585–588. https://doi.org/doi:10.1016/j.ssi.2004.03.045.
316 [43] T. Sato, S. Imaeda, K. Sato, Thermal transformation of yttrium hydroxides to yttrium oxides,
317 Thermochimica Acta. 133 (1988) 79–85. https://doi.org/10.1016/0040-6031(88)87140-5.
318 [44] F. Demoisson, R. Piolet, F. Bernard, Hydrothermal growth of ZnO nanostructures in
319 supercritical domain: Effect of the metal salt concentration (Zn(NO3)2) in alkali medium
320 (KOH), The Journal of Supercritical Fluids. 97 (2015) 268–274.
321 https://doi.org/10.1016/j.supflu.2014.12.012.

322

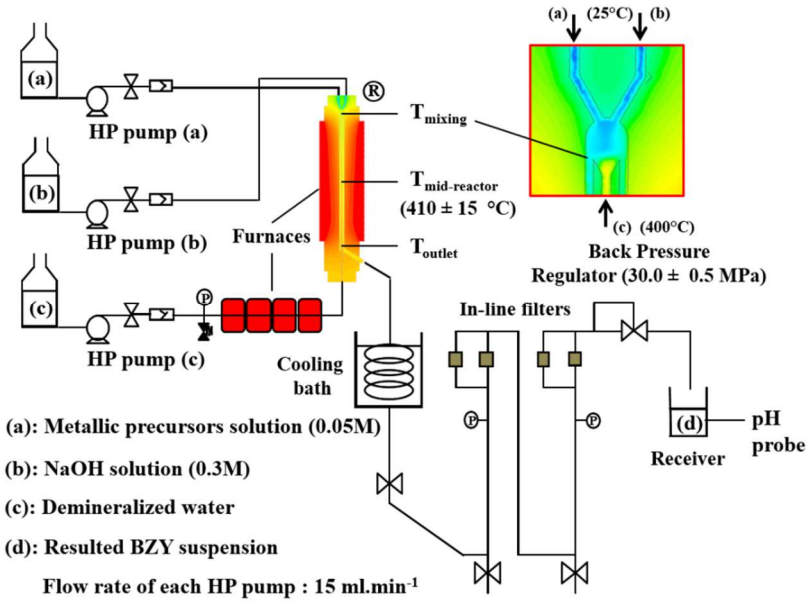

323

324 **Figure 1.** Schematic of the continuous hydrothermal set-up (adapted from[44]) (*Not colored*

325 *for the print version*)

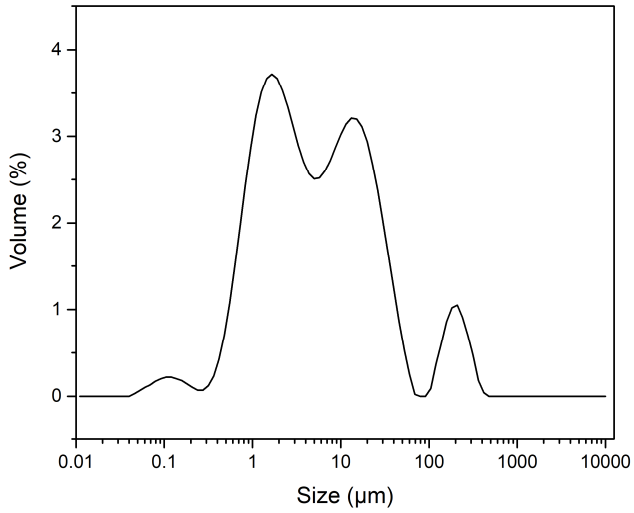

326

327 **Figure 2.** Particle size distribution by volume of the powder synthesized by the continuous

328 hydrothermal process

329

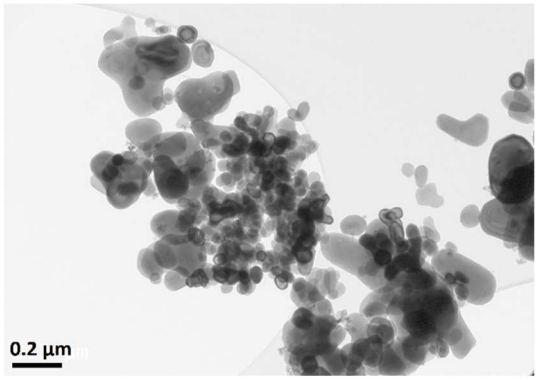

Figure 3. TEM micrograph of the BZY powder synthesized by continuous hydrothermal process

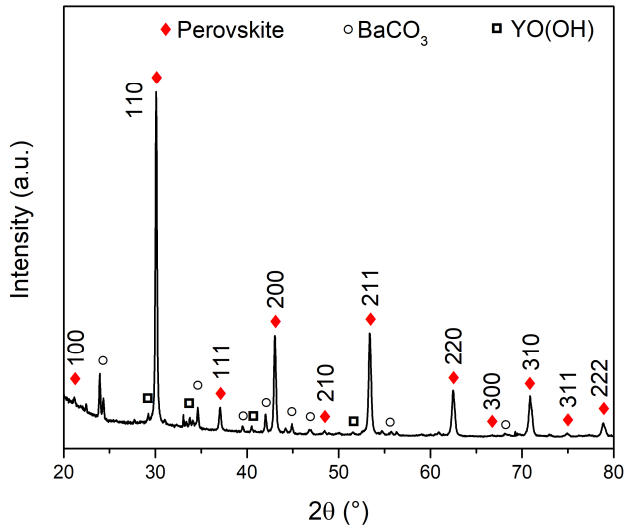

Figure 4. X-ray diffractogram of the BZY powder synthesized by continuous hydrothermal process (*Not colored for the print version*)

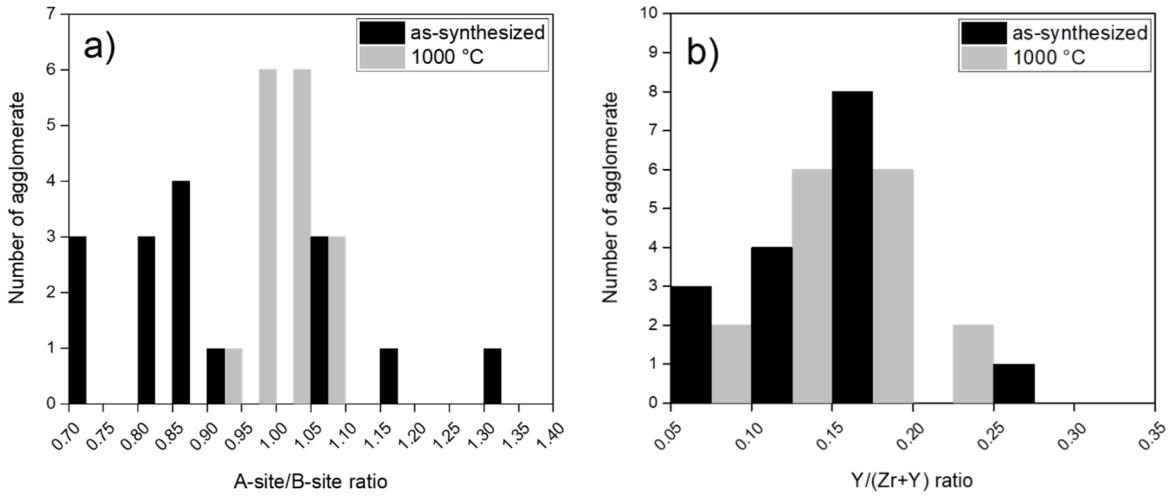

339

340 **Figure 5.** a) A-site/B-site ratios and b) Y/(Zr+Y) ratios obtained from EDX measurement on
341 the as-synthesized powder and on the powder annealed at 1000 °C and the corresponding number
342 of agglomerates per interval.

343